11^{th} International Conference on Fracture Mechanics of Concrete and Concrete Structures
FraMCoS-11
J. M. Chandra Kishen, A. Ramaswamy, S. Ray and R. Vidyasagar (Eds)
https://doi.org/10.21012/FC11.092312

MODELLING OF DAMAGE PROCESSES IN CONCRETE UNDER MONOTONIC AND CYCLIC LOADING

Vladislav Gudžulić[1,*], Koussay Daadouch[1] and Günther Meschke[1]

[1]Ruhr-University Bochum, Germany
e-mail: vladislav.gudzulic@ruhr-uni-bochum.de

Key words: Cohesive Fracture, Fiber Reinforced Concrete, Cyclic loading, Hysteresis

Abstract. Concrete is one of the most commonly utilized building materials and has a significant environmental footprint due to its production process. Over the past decades, considerable progress has been made in developing high-performance and ultra-high-performance concretes and incorporating fiber reinforcements in structural concrete, resulting in improved strength and durability, and opening the possibility of creating slenderer structures leading to significant material savings. However, adequate models and design approaches must accompany these material improvements to fully realize the potential benefits, especially considering the effects of the long-term sustained loads.
This work focuses on material behavior aspect of plain and fiber-reinforced high-performance concrete, investigating damage processes and mechanisms occurring at small scales, which are not readily observable during loading tests. To this end, it presents a framework for generating mesoscale concrete models based on virtually created aggregate and fiber distributions [1] and Computational Tomography (CT) images. A finite element model utilizing zero-thickness interface elements is applied to simulate the fracture of concrete specimens on the laboratory scale. The zero-thickness interface elements are equipped with a cohesive-frictional traction-separation law a model for hysteresis occurring due to incomplete crack closure during loading-unloading cycles [2]. The steel fibers are considered explicitly and modeled as elastoplastic Timoshenko beam elements. The 3D elastoplastic constitutive law with isotropic is adapted for beam elements by iterative solution of zero stress constraints via Newton's method [3]. The embedment of fibers into the cement matrix is facilitated via a penalty-based frictional tying algorithm that enables flexible placement of fibers without needing to conform with the background mesh. The bond between the cement matrix and fibers is modeled via an elastoplastic bond-slip law proposed in [4], whose parameters are calibrated based on single-fiber pullout experiments. All model components are implemented into the open-source Finite Element program "Kratos Multi-physics" [5]. The capabilities of the proposed model are demonstrated by reanalyzing several experimental scenarios, such as notched prismatic specimens under uniaxial tension [6] and comparing results with the available experimental data.

1 INTRODUCTION

Concrete, the second most utilized substance worldwide after water, plays a central role in the construction industry. Its primary ingredient, cement, is the most produced material on Earth by mass [7]. However, the production of cement and concrete contributes significantly to CO_2 emissions. Although the cement industry has made commendable strides in reducing CO_2 emissions through improved energy efficiency and the adoption of alternative fuels, it remains imperative to further decrease emissions to meet the growing demand for cement-based materials in the years ahead. Optimizing

the design mixes to obtain high- and ultra-high-performance concrete (HPC and UHPC, respectively) is an attractive option that reduces the total cement consumption [7].
Further, high- and ultra-high- performance concrete enable more architectural freedom to design slender, aesthetically pleasing, and sustainable constructions. The addition of fibers to the mix typically enhances the durability [8] and impact resistance of such concretes [9]. Also, it is well known that fiber-reinforced concrete fails in a much more ductile way [8], allowing more time for safe evacuations in emergency situations. Another critical issue is the behavior of HPC and UHPC under short- and long-term cyclic loading, which has been investigated in the past (see, e.g., [10]), but such a complex processes are difficult to investigate purely experimentally and still not completely understood. Therefore, this is an ideal use-case for numerical modeling, where a virtual-lab environment can be set up and utilized to repeat experiments virtually, having full control of the input and measured values. This paper presents the framework for establishing a virtual lab environment encompassing the mesoscale finite element model generation on basis of CT-image (section 2), discrete fiber formulation and the computational model for fracture (section 3) which are implemented into the open-source Finite Element program "Kratos Multi-physics" [5]. The section 4 focuses on detailed analysis and modeling of the damage processes in high-performance concretes at a mesoscale level. Two specific cases are investigated: a double-notched prismatic HPSFRC specimen subjected to cyclic tensile loading and a cylindrical HPSFRC specimen subjected to monotonic compressive loading. These investigations aim to unravel the role of interaction between individual mesoscopic components in producing the complex macroscopic response, thereby enhancing our understanding and interpretation of experimental results.

2 CT-IMAGE-BASED MODEL GENERATION

In order to study the fracture processes within a virtual laboratory environment, it is essential to faithfully simulate the mesoscale characteristics of the concrete specimen. The main task involves capturing the heterogeneity in stiffness caused by coarse aggregates, as most of the damage processes at this scale are majorly influenced by it. To this end, a computational tomography (CT) scan was performed on a small cylindrical specimen with a diameter $\varnothing$39.56mm and a height h = 35.42mm. Utilizing the resulting 3D image (see Figure 1a), a finite element mesh including coarse aggregate, fiber and mortar matrix phases was generated for further analysis and investigation.

2.1 Modeling the aggregates

The first step of the model generation is image processing, during which the aggregates are segmented from the original CT image. The image thresholding technique proved very effective for obtaining a preliminary segmentation of the aggregates, represented by the set of voxels in the original image corresponding to aggregates (Figure 1b). Such segmentation usually requires further processing due to noise in the CT image and the possibility that some aggregates might be "touching" (sharing voxels). Therefore, we refine the segmentation by applying image processing tools such as image erosion and dilation. Then by applying a watershed transformation [11], we can obtain a separate representation for each aggregate (Figure 1c). The next step is to convert the image into geometry by a suitable triangulation technique. We start by creating the geometry of individual aggregates. A point is created on the corner of every voxel of the aggregate. Then the convex hull triangulation of these points [12] is obtained, which encloses the aggregate and represents a good approximation of its surface geometry (Figure 1d). To generate the mesh, the geometry of the matrix has to be defined, which is, in this case, a cylinder. The aggregates are

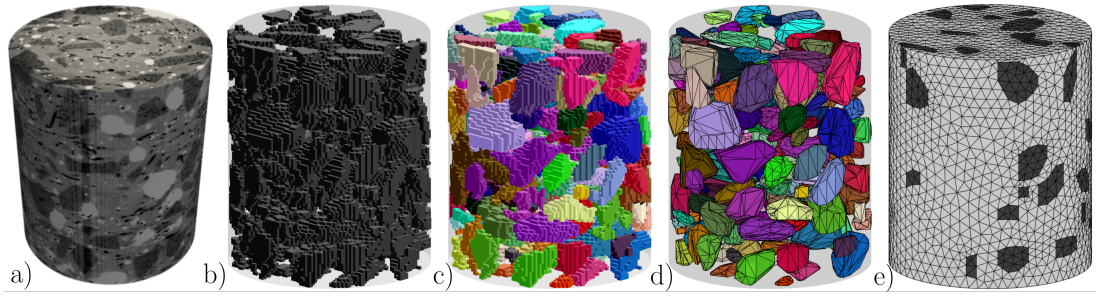

Figure 1: Stages of generating the computational model: a) Original CT image of an actual specimen with 4 phases: fibers (black), aggregates (dark grey), mortar matrix (grey), and air pores (light grey). b) Preliminary segmentation of the aggregates. c) Separated segmentation of the aggregates. d) Surface triangulations of individual aggregates. e) Final tetrahedral mesh with two sets of elements representing aggregates (dark grey) and mortar (light grey).

introduced to the cylinder by applying Boolean operations on both geometries: aggregates and a cylinder. The resulting geometry is meshed with tetrahedral elements of user-defined size and order. Figure 1e shows the mesh of two sets of elements, representing two different phases (aggregates in dark grey and mortar in light grey). Boolean operations and mesh generation are performed using open-source geometry and mesh processing tool gmsh [13].

2.2 Modeling the fibers

Similar to the case of aggregates, a preliminary segmentation of fibers is obtained through image thresholding followed by image refinement. Unlike the aggregates, fibers are more prone to clumping and forming clusters of overlapping fibers (Figure 2a). However, watershed transformation cannot separate the overlapping fibers, as minor dents or noise along the length of a single fiber trigger the watershed transformation to falsely split the fiber. Hence, we propose the following algorithm to separate the clusters and reconstruct each fiber. First, we skeletonize the segmented voxels that represent fiber material. Then we can identify the branch points (in blue) (Figure 2b). By removing the branch points, we separate the cluster into individual pieces of fibers (Figure 2c). To reconstruct the actual fibers, we compute the orientation vector of each piece, then by comparing the orientations of neighboring pieces, it can be identified whether two pieces belong to the same fiber or not. Finally, assuming the fibers are straight, a line connecting the assembled pieces' endpoints defines the fiber (Figure 2d). The lines representing the fibers are imported into the Finite Element analysis software where they are discretized with linear Timoshenko beam elements, assigned the appropriate material properties, and embedded into the background mesh.

3 MODEL FORMULATION

In this work, two modeling strategies are presented. In one, concrete is assumed homogeneous, whereas the fibers are discretely resolved, and in the other, a full mesoscale representation, including explicit representation of coarse aggregates, mortar matrix, and fibers has been adopted (see Section 4).

3.1 Discrete Crack Model

Depending on the resolution, the matrix material (concrete or mortar) is assumed to be a homogeneous continuous medium, discretized by solid tetrahedral finite elements with four nodes (T4), assumed to behave in a linear elastic manner. Cracking of the matrix is modeled discretely using the cohesive zero-thickness interfaces elements as in [6, 14, 15]. The zero-thickness interface elements are inserted between solid elements and they represent crack surfaces. The interface element kinematics are defined according to the local coordinate system x'-y'-z'

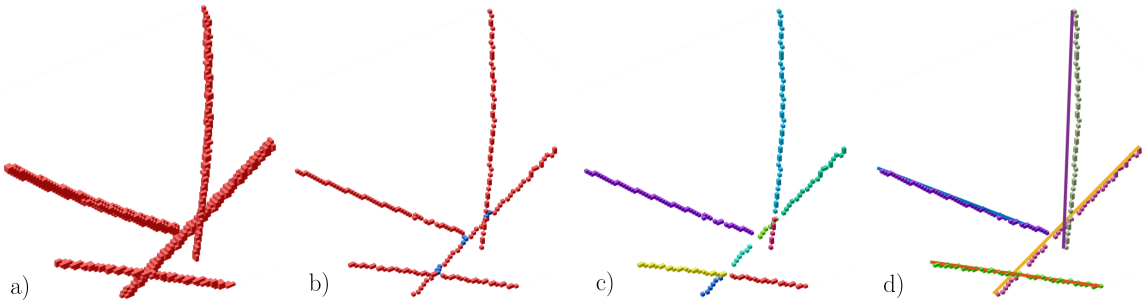

Figure 2: Stages of reconstructing fibers: a) An initial segmentation of a cluster of four overlapping fibers. b) Skeletonization of the segmented fiber voxels. Branch points are marked in blue. c) Splitting fibers into segments at intersection points. d) Reconstructed fibers are represented by straight lines connecting the endpoints of segmentation pieces that belong to their corresponding fiber.

and node numbering as illustrated in Figure 3.

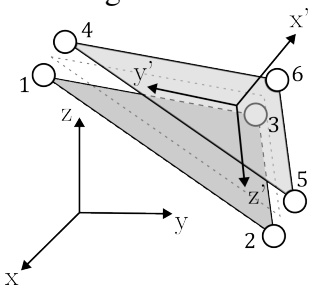

Figure 3: Definition of the global and local coordinate systems and node numbering convention for a linear zero-thickness interface element.

The local coordinate x' always points in direction of the normal ($\mathbf{n}$) to the middle surface of the interface element and the coordinates y' and z' are defined so that they lie in the plane of the middle surface, parallel to arbitrary defined unit vectors $\mathbf{t}$ and $\mathbf{s}$, satisfying the relation $\mathbf{n} = \mathbf{t} \times \mathbf{s}$. The crack opening in the local coordinate system is defined as:

$$[\![\mathbf{u}]\!]' = \mathbf{R}[\![\mathbf{u}]\!], \tag{1}$$

where $\mathbf{R}$ is the rotation matrix, and $[\![\mathbf{u}]\!] = \mathbf{N}_u\mathbf{u}$ is the crack opening vector in the global coordinate system, obtained by a product of nodal displacements ($\mathbf{u}$) and matrix containing shape functions ($\mathbf{N}_u$) of the interface element (see e.g., [2] for details). The relationship between traction vector (in local coordinate system of the interface element) acting on the middle surface of interface element ($\mathbf{t}'_c$, subscript c denoting cohesive) and the continuum stress tensor ($\boldsymbol{\sigma}$) is defined as follows:

$$\mathbf{t}'_c = \begin{bmatrix} t_{cx'} \\ t_{cy'} \\ t_{cz'} \end{bmatrix} = \mathbf{R}(\boldsymbol{\sigma} \cdot \mathbf{n}). \tag{2}$$

The failure surface in the traction space, illustrated in Figure 4 is defined as:

$$\hat{F}_c(\mathbf{t}, q_c) = \bar{t}_c - q_c \leq 0, \tag{3}$$

where $\bar{t}_c(\mathbf{t}) = \sqrt{t^2_{cx'} + \frac{1}{\beta^2}(t^2_{cy'} + t^2_{cz'})}$ is the effective traction [14], and $q_c(\alpha_{c,max})$ is the strength of the material point, depending on the stress history through $\alpha_{c,max}$. The softening law $q_c(\alpha_{c,max})$ is defined by the expression:

$$q_c(\alpha_{c,max}) = f_{tu} e^{-\frac{f_{tu}}{G_{F,I}}(\alpha_{c,max})}, \tag{4}$$

where f_{tu} is the tensile strength, $G_{F,I}$ is the fracture energy for mode I cracks, and $\alpha_{c,max} = \max_{t\in[0,T]}(\alpha_c(t))$ is the maximal value of $\alpha_c = \sqrt{[\![u_{x'}]\!]^2 + \frac{\beta^2}{\kappa^2}([\![u_{y'}]\!]^2 + [\![u_{z'}]\!]^2)}$ experienced by the material point from the beginning of the simulation ($t = 0$) to the current time ($t = T$). The parameters β and κ appearing in the above expressions denote the values of the ratio of shear to tensile strength ($\beta = \frac{f_{su}}{f_{tu}}$) and the ratio of fracture energies in mode II and mode I ($\kappa = \frac{G_{F,II}}{G_{F,I}}$), respectively [15]. Consequently, the damage parameter is defined as:

$$d_c = 1 - \frac{q_c}{K_c \alpha_{c,max}}, \tag{5}$$

with K_c being the penalty parameter that ties the undamaged surfaces of the interface

element together, and gets fully recovered upon closure of the crack. The loading-unloading behavior is illustrated in Figure 5.

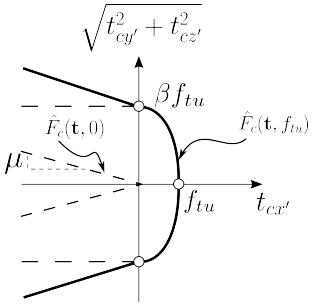

Figure 4: Failure surface defined in traction space (see axes convention in Figure 3). After damage is initiated, the failure surface gradually shrinks to the frictional cone whose inclination is defined by the friction coefficient μ.

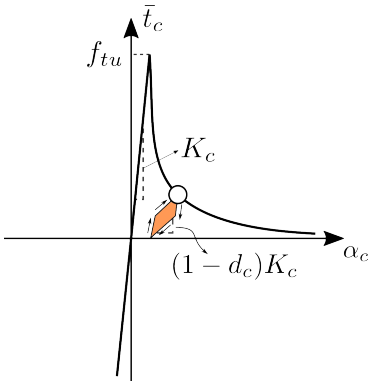

Figure 5: The exponential softening law with unloading/reloading hysteresis.

In addition to cracking, the processes of frictional sliding between crack faces and incomplete closure of cracks majorly influence the overall macroscopic response in terms of force-displacement diagrams. These processes are included through additional terms conditionally appearing in the traction-separation law. The frictional sliding occurs when already initiated cracks are closed and experience compressive and shear stresses. Figure 6 illustrates three stages of crack development (intact, bridging and completely open crack). By bridging, it is assumed that the separation between the crack faces is not yet complete, but there are some particles and matrix ligaments that still provide residual strength to the crack. The degradation of this residual strength is modeled by the exponential softening law, defined by the Eqs. 4 and 5. We assume that the frictional sliding can only occur between the crack faces where the damage has already occured, meaning that we use the damage parameter d_c to denote the fraction of the interface element that has already been fully cracked. Hence, the frictional contribution is defined as:

$$\mathbf{t}_{f'} = K_c \begin{bmatrix} 0 \\ [\![u_{y'}]\!] - [\![u_{y'}]\!]_p \\ [\![u_{z'}]\!] - [\![u_{z'}]\!]_p \end{bmatrix} H([\![u_{x'}]\!]), \qquad (6)$$

where $H([\![u_{x'}]\!])$ is the friction activation function (Heaviside function), such that $H([\![u_{x'}]\!]) = 1$, when $[\![u_{x'}]\!] \leq 0$, and $H([\![u_{x'}]\!]) = 0$ otherwise. Note that the case $[\![u_{x'}]\!] < 0$ is physically not admissible, however, due to use of penalty contact enforcement, it is possible that in numerical analysis small penetration inversely proportional to the value of the penalty parameter (K_c) occurs. As can be seen from Eq. 6, the friction is modeled using the framework of plasticity. The frictional yield function (g) is defined as:

$$g(\mathbf{t}_{f'}) = \|\mathbf{t}_{f'}\| - \mu\|\langle -t_{cx'}\rangle\|, \qquad (7)$$

where $\langle . \rangle$ denotes Macaulay bracket. The frictional sliding problem is essentially 1D problem, so for the case of slipping ($g > 0$), evolution of plastic strains can be solved in a closed form by rephrasing the meaning of the frictional slip multiplier $\dot{\hat{\gamma}}_f = \dot{\gamma}_f / \|\mathbf{t}_{f'}\|$, as proposed in [16].

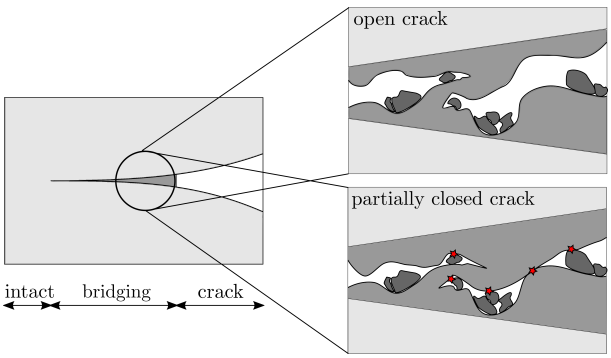

Figure 6: Cohesive crack model (left): distinguishing intact, partially damaged, and completely damaged part. Crack closure model (right): Contact between the asperities is indicated by the red stars in the illustration [6].

The final component of the constitutive model is the submodel for incomplete crack closure. The basic idea is illustrated in Figure 6. The cracks in concrete are rough, and many small particles contaminate the crack surface. Upon closure, these asperities come into contact before the crack is nominally closed, resulting in partial recovery of the stiffness. After certain level of stress (σ^{cl}) has been achieved, the sliding between these asperities activates, and the rough crack surfaces slide until they fit with each other. This is modeled using 1D plasticity with two distinctive yield functions for upper and lower stress:

$$\begin{aligned} h_1 &= t_{x'} \leq 0 \\ h_2 &= -t_{x'} + \sigma^{cl} \leq 0, \end{aligned} \tag{8}$$

where σ^{cl} is the closure stress that needs to be overcome before the crack can be closed. The value of σ^{cl} naturally depends on the current crack opening, since for very large openings there should be no resistance to closure, and for very small openings the resistance to closure is high. This is controlled by a state equation $\sigma^{cl} = \sigma_{ref}[\![u_{x'}]\!]_{ref}/([\![u_{x'}]\!] + b[\![u_{x'}]\!]_{ref})$ [2], with σ_{ref} and $[\![u_{x'}]\!]_{ref}$ are material parameters, and b is a very small number ($\sim 10^{-5}$) to avoid division by zero. The closure traction ($\mathbf{t}_{cl'}$) developing inside of the crack during the process of closure manifests itself as a hysteresis in the force-displacement response (see Figure 5) and is calculated as (see [2] for more details):

$$\mathbf{t}_{cl'} = K_c \begin{bmatrix} [\![u_{x'}]\!] - [\![u_{x'}]\!]_p \\ 0 \\ 0 \end{bmatrix}. \tag{9}$$

The traction acting on the middle surface of the interface element is, finally, defined as:

$$\mathbf{t}' = (1-d_c)K_c \begin{bmatrix} [\![u_{x'}]\!] \\ \frac{\beta^2}{\kappa}[\![u_{y'}]\!] \\ \frac{\beta^2}{\kappa}[\![u_{z'}]\!] \end{bmatrix} + d_c(\mathbf{t}_{f'} + \mathbf{t}_{cl'}). \tag{10}$$

The simulations are fairly expensive because they involve duplication of the nodes between solid elements where interfaces are inserted. Typically, the final mesh, where interface elements are inserted between all solid elements, contains 4-6 (2D) and 8-12 (3D) times more nodes than the original tetrahedral mesh. To alleviate this issue, we implemented an adaptive insertion algorithm [17] that inserts interface elements on-the-fly, during simulation, only in the needed locations shortly before the fracturing is initiated. The insertion is activated when the criterion that the effective traction is greater than a portion of tensile strength is fulfilled: $\bar{t}_c(\mathbf{t}) \geq \omega f_{tu}$, where ω is the insertion factor (typically 0.6-0.8) and f_{tu} is the tensile strength.

3.2 Discrete Fiber Model

The fibers in this work are modeled explicitly as linear Timoshenko beam elements [18]. A reduced integration scheme with a single Gauss point alleviates the shear locking [19] inherent to this element's formulation. Additionally, the computational cost is reduced, which is crucial when dealing with a large number of explicit fibers.

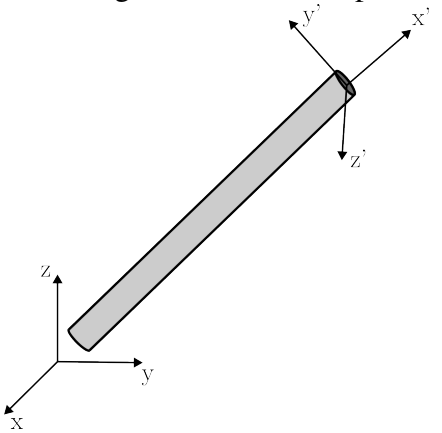

Figure 7: Definition of the local (x'–y'–z') and global (x–y–z) axes of the linear Timoshenko beam element.

The linear Timoshenko beam elements in 3D have six degrees of freedom (DOFs) per node. These are three translations (u_x, u_y, and u_z) and three rotations (φ_x, φ_y, and φ_z), all defined in the global coordinate system. The generalized strains are calculated from displacements and rotations according to [18]. The fibers are bridging open cracks due to relatively large sliding of the crack faces, and therefore experience

large deformations that lead to plastic hinge formation, which affects the fibers' crack-bridging properties. A 3D constitutive law is implemented at integration points of the fiber cross-section and these stresses are then integrated to obtain the generalized stresses or stress resultants (N_x, Q_y, Q_z, M_x, M_y, M_z). Specifically, an elastoplastic law of Von-Mises type with exponential isotropic hardening has been implemented for modeling steel fibers. The yield function is defined as:

$$f = \sqrt{\frac{3}{2}\boldsymbol{\sigma}_{dev} : \boldsymbol{\sigma}_{dev}} - \sigma_y - (\sigma_{inf} - \sigma_y)(1 - e^{-\eta\alpha}), \tag{11}$$

where $\boldsymbol{\sigma}_{dev}$ is the deviatoric part of the total stress tensor $\boldsymbol{\sigma}$, σ_y is the initial yield stress, σ_{inf} is the final yield stress, η is the material parameter that controls the nonlinear hardening slope, and α is the strain-like internal variable. The flow rule is assumed associative, hence the evolution of plastic strains is defined as:

$$\dot{\boldsymbol{\varepsilon}}_p = \dot{\gamma}\frac{\partial f(\boldsymbol{\sigma}, \alpha)}{\partial \boldsymbol{\sigma}}, \tag{12}$$

and the evolution of the strain-like internal variable α is:

$$\dot{\alpha} = \sqrt{\frac{2}{3}}\dot{\gamma}, \tag{13}$$

with $\dot{\gamma}$ being the plastic slip multiplier. The above equations and Karush-Kuhn-Tucker optimality conditions are solved using the standard radial return map procedure (see, e.g., [24]). Due to the modeling assumptions of the beam theory, there are additional constraints that the stress tensor needs to satisfy, namely, the stress components in the local coordinate system of the beam element $\sigma_{y'y'}$, $\sigma_{z'z'}$, and $\tau_{y'z'}$ need to be zero (see Figure 7 for axes convention). These constraints are enforced using an iterative procedure proposed by Klinkel and Govindjee [3] and will be omitted here for the sake of brevity.

3.3 Bond between Fibers and Solid elements

To establish a connection between the fibers, which are discretized by linear Timoshenko beam elements, and the background finite element mesh of the bulk material, a penalty-based frictional tying algorithm is utilized. First, a search for every fiber is performed to find on which solid element it lies (note that it can lie also on the surface, edge, or vertex shared by multiple solid element, in which case it gets tied to all these solid elements) and the isoparametric coordinates $\boldsymbol{\xi}$ of the fiber node point are evaluated for this element. Next, a bond element is created to establish the relationship between the background solid element, the fiber node, and the segments of the fiber passing through the node. This bond element contains information about the solid element, fiber node, and the relevant fiber segments. Using this information, a rotation matrix $\mathbf{R}_{bond}$ is calculated for the bond. The point of the solid element that coincides with the fiber node is connected to the fiber node using three stiff springs, facilitating the coupling between the two elements. These springs are oriented to align with the local coordinate system of the bond. Among the three springs, the one parallel to the fiber is equipped with an elastoplastic law, while the two lateral springs are elastic. Knowing the shape functions ($\mathbf{N}(\boldsymbol{\xi})$) and the nodal displacements ($\hat{\mathbf{u}}$) of the solid element, the relative slip is calculated as follows:

$$[\![\mathbf{u}]\!]'_{bond} = \mathbf{R}_{bond}(\mathbf{u}_{solid}(\boldsymbol{\xi}) - \mathbf{u}_{fiber}), \tag{14}$$

where $\mathbf{u}_{solid}(\boldsymbol{\xi}) = \mathbf{N}(\boldsymbol{\xi})\hat{\mathbf{u}}$ and $\mathbf{u}_{fiber}$ is the displacement vector of the fiber node. The component of $[\![\mathbf{u}]\!]'_{bond}$ in the x' direction represents the slip between the fiber and the solid matrix and it is denoted as s. The bond-slip law illustrated in Figure 8 is given as follows:

$$\tau_y = \begin{cases} \tau_{max} + \mu t_N, & s \leq s_0 \\ \tau_{max} + \mu t_N, & s_0 < s \leq s_1 \\ \tau_0 + (\tau_{max} - \tau_0)e^{\frac{s_1 - s}{s_{ref}}} + \mu t_N, & s > s_1, \end{cases} \tag{15}$$

where $t_N = \sqrt{t^2_{y',bond} + t^2_{z',bond}}$ is the lateral pressure that the fiber is exerting on the matrix through two lateral (elastic) springs.

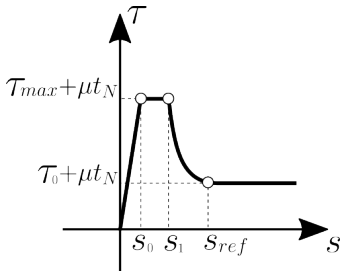

Figure 8: Illustration of the fiber bond-slip law with interpretation of material parameters.

4 NUMERICAL SIMULATIONS ON THE LABORATORY SCALE

This section presents the validation examples for the proposed modeling framework, as well as the discussion of the obtained computational results. Two experimental setups have been numerically reanalyzed: a double-notch prismatic HPSFRC specimen subjected to cyclic tension and an HPSFRC cylindrical specimen subjected to monotonic compression. In both analyses, the Dramix OL 6/0.16 short steel fibers have been used. Their geometrical and material properties are given in Table 1. For both simulations, the bond properties listed in Table 2 have been used.

Table 1: Properties of Dramix OL 6/0.16 fibers

Material Property		Fibers
Length	[mm]	6
Diameter	[mm]	0.16
Yield strength (σ_y)	[MPa]	2200
Ultimate strength (σ_{inf})	[MPa]	2600
Hardening exponent (η)	[MPa]	10

4.1 Notched prismatic concrete specimen under cyclic tension

The experimental data for this example have been published in [6], and here the numerical reanalysis of the boundary value problem, using the improved model for discrete fibers, is presented. The double-notched prismatic specimen of dimensions $140 \times 40 \times 40\text{mm}^3$ with two notches on the side (height of 5mm and depth of 10mm), illustrated in Figure 9, has been subjected to displacement-controlled cyclic tensile loading. The material properties of HPSFRC are listed in Table 3.

Table 2: Properties of the fiber-HPC bond

Material Property		Bond
τ_{max}	[MPa]	4.0
τ_0	[MPa]	8.0
s_0	[mm]	0.0004
s_1	[mm]	0.0004
s_{ref}	[mm]	0.1
Friction coefficient (μ)	[-]	0.6

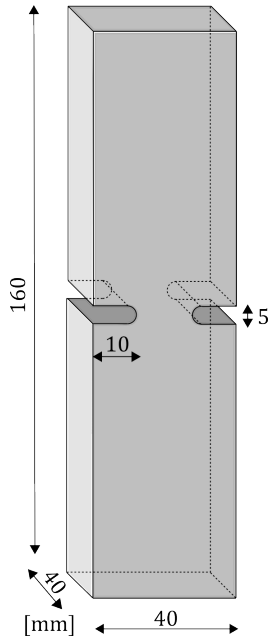

Figure 9: Dimensions of the double-notched prism specimen in mm. The displacement degrees of freedom of the bottom and the top surface are fixed in all directions, and the displacement in vertical direction is prescribed at the top surface.

The loading protocol in the numerical simulation is set up in the following way. The specimen was subjected a monotonic tensile loading until the first crack appeared. Afterwards, the load was reduced to 10% of the nominal tensile strength, and the change in length (Δl) was recorded. The vertical displacement was then subsequently reapplied to the upper end of the specimen until the crack mouth opening displacement value measured at the notch area matched $\text{CMOD}_1 = 2\Delta\text{l}$. The process of controlled loading, causing crack opening, and unloading was then repeated until the final crack mouth opening displacement

reached $\text{CMOD}_n = 10\Delta l$. Figure 10 illustrates the experimental and simulated force-crack mouth opening displacement (CMOD) responses. After reaching the peak load, a significant drop in load occurs, followed by stabilization at a residual level. This drop corresponds to the development of a crack in the notched area of the concrete specimen (see Figure 11). Once the crack is fully formed, the fibers contribute to the residual strength. Both in experiments and the simulation, it is noticeable that there is relatively small hysteresis during loading/reloading cycles. This can be attributed to the fact that the fibers primarily provide the residual carrying capacity, and the dissipation is mainly caused by the sliding of fibers back and forth within the fiber channels.

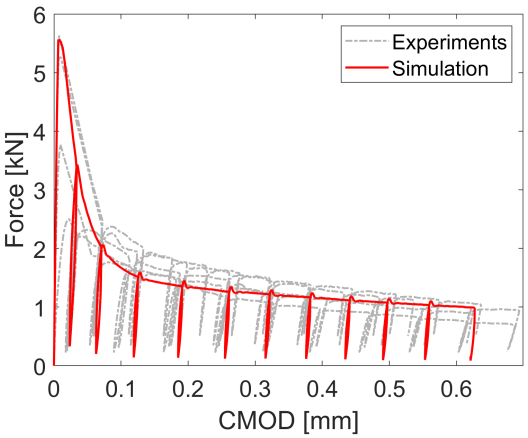

Figure 10: Force-CMOD response of the double-notched prismatic HPSFRC specimen subjected to cyclic tensile loading.

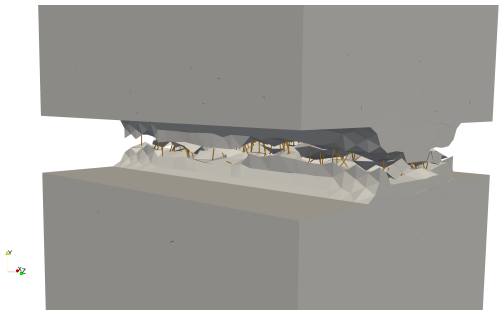

Figure 11: A single crack formed at the notch of the prism. The fiber bridge the crack faces and provide the residual strength to the specimen. Deformations are scaled tenfold.

4.2 Small cylindrical specimen under compression

In this subsection, a mesoscale finite element model of a cylindrical specimen with dimensions ⌀39.56mm, h = 35.42mm, generated from the CT-Image using the methodology described in section 2, was numerically analyzed. The geometry of the considered boundary value problem is shown in Figure 12. The degrees of freedom of the top and bottom surfaces of the cylinder are completely fixed, and the displacement in the vertical direction is prescribed on the top surface. The material parameters of all constituents used in simulation are provided in Table 3. Note that the values were taken from the literature where the measurements were unavailable. In this example, only the aggregates that would pass through the sieve of the size of 2mm were explicitly resolved, corresponding to the volume fraction of 26.7%. Therefore, to match elasticity parameters to the macroscopically measured values, Young's modulus value for basalt was chosen as 57.5 GPa, and the Poisson's ratio was selected as 0.25, which are within the range of measured values in [23]. It should also be noted that the interface transition zone (ITZ) between coarse aggregates and mortar matrix is also explicitly modeled, however, due to lack of experimental data, the material properties of ITZ are taken same as for the mortar matrix.

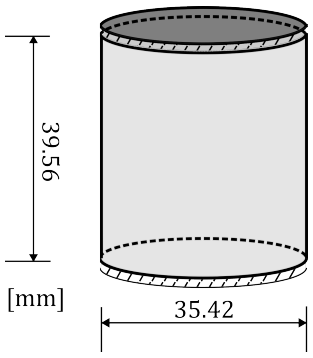

Figure 12: Dimensions of the cylindrical specimen in mm. The displacement degrees of freedom of the bottom and the top surface are fixed in all directions, and the displacement in vertical direction is prescribed at the top surface.

Table 3: Material properties for aggregates and high-performance mortar, and high-performance concrete

Material Property		**Basalt**	**Mortar (HPC-02)**	**Concrete (HPC-08)**
Tensile strength (f_t)	[MPa]	14.0 [23]	5.7	6.2
Young's modulus	[MPa]	57500.0	39183.0	43224.4
Poisson's ratio	[-]	0.28 [23]	0.2	0.21
Fracture energy	$[\frac{\text{N}}{\text{mm}}]$	0.125	0.05	0.1
Friction coefficient	[-]	0.7	0.7	0.7
Ref. closure stress	[MPa]	-	-	6.2
Ref. crack opening	[mm]	-	-	0.004

The comparison between the experimentally measured and simulated force-displacement response is shown in Figure 13. Due to irregularities at the top and bottom surfaces of the specimen, the contact between the loading plate and the specimen was gradually established, resulting in a nonlinear loading path. Hence, the experimental diagram was shifted so that the zero displacement corresponds to the point where the contact was fully established. Nevertheless, the agreement between the experimental and numerical results can be considered satisfactory, considering that the simulation results emerge from the interactions between elementary components (aggregates, fibers and the mortar matrix). It can be observed that the experimental peak load occurs at the displacement of 230µm, which corresponds to a strain of 5.81 ‰, a ductility that surpasses the usual value for plain concrete of $\sim$ 2–3‰ [21], clearly a consequence of the presence of short steel fibers. The same effect is observed in numerical simulation with the peak load occurring at around 200µm, corresponding to a strain of 5.06‰. The numerical simulation showed that most of the short steel fibers bridging the open cracks have fully formed plastic hinges, dissipating the energy while slowing the crack growth and delaying the localization process.

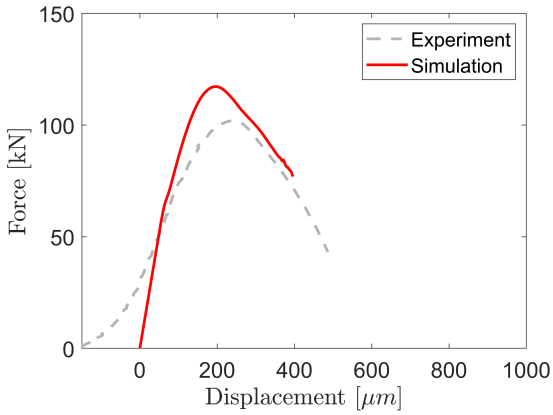

Figure 13: Comparison of the experimental and simulated force-displacement diagrams for the cylindrical HPSFRC specimen under monotonic compressive loading.

Figure 14 shows the cracking pattern at the last step before the numerical divergence occurred. The formation of the hourglass failure mode is evident, influenced by the strong multiaxial stress caused by fixed boundary displacements at the specimen's top and bottom surfaces. The radial extent of spalled concrete reaches approximately a quarter of the specimen's measured radius. The cracking pattern confirms that the numerical simulations accurately capture the failure mode, with initially tension-opening vertical or slightly inclined cracks influenced by the mesostructure topology. As the ultimate load is reached, deformations localize due to shear sliding of these cracks under high vertical compressive stress.

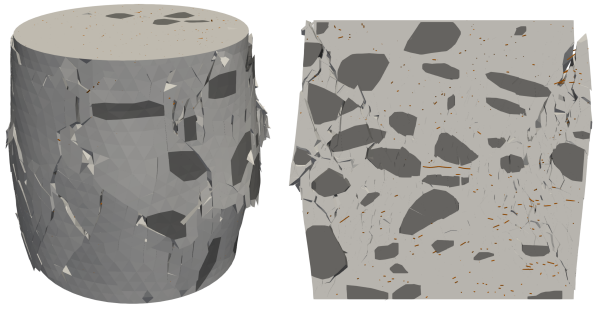

Figure 14: Cracking pattern of the cylinder subjected to monotonic compression at the last converged step. Deformations are scaled tenfold.

5 CONCLUSIONS AND OUTLOOK

This paper presents a comprehensive virtual-lab framework that utilizes 3D CT-based images to generate finite element models and solve boundary value problems. The two numerical simulations showcased in this work demonstrate the utility of the virtual lab concept in enhancing the interpretation of experimental data. By examining the interactions between individual components, a deeper understanding of the complex material behavior of HPSFRC is achieved. However, there are areas for improvement. For instance, simulations involving complex multi-axial stress states, such as the mesoscale analysis of concrete cylinders under compression, encountered convergence issues beyond the peak load. Additionally, the virtual lab should incorporate models for creep and fatigue behavior, which are currently being developed, to investigate specimens subjected to long-term loading.

6 ACKNOWLEDGMENTS

Financial support for this work was provided by the German Research Foundation (DFG) within the Priority Program 2020 ”Cyclic deterioration of High-Performance Concrete in an experimental-virtual lab” (Project 353819637). This support is gratefully acknowledged. The authors also want to thank Mr. Niklas Schäfer, and Prof. Rolf Breitenbücher from the Chair of Building Materials at Ruhr-University Bochum, for providing the experimental data used in this contribution and Mr. Dietmar Meinel from Bundesanstalt für Materialforschung und -prüfung (BAM) for performing CT scans of the cylindrical specimen.

REFERENCES

[1] Holla, V. and Vu, G. and Timothy, J. J. and Diewald, F. and Gehlen, C. and Meschke, G. 2021. Computational generation of virtual concrete mesostructures. *Materials* **14**:3782.

[2] Gudžulić, V. and Meschke, G. 2021. Multi-level approach for modelling the post-cracking response of steel fibre reinforced concrete under monotonic and cyclic loading. *PAMM* **21**: e202100194.

[3] Klinkel, S. and Govindjee, S. 2002. Using finite strain 3D-material models in beam and shell elements. *Engineering Computations* **19**:254–271.

[4] Zhan, Y. and Meschke, G. 2014. Analytical model for the pullout behavior of straight and hooked-end steel fibers. *Journal of Engineering Mechanics* **12**:04014091.

[5] Dadvand, P. and Rossi, R. and Oñate, E. 2010. An object-oriented environment for developing finite element codes for multi-disciplinary applications. *Archives of Computational Methods in Engineering* **17**:253–297.

[6] Schäfer, N. and Gudžulić, V. and Breitenbücher, R. and Meschke, G. 2021. Experimental and numerical investigations on high performance SFRC: Cyclic tensile loading and fatigue. *Materials* **14**:7593.

[7] Scrivener, K. L. and John, V. M. and Gartner, E. M. 2018. Eco-efficient cements: Potential economically viable solutions for a low-CO2 cement-based materials industry. *Cement and Concrete Research* **114**:2–26.

[8] Frazão C. and Camões A. and Barros, J. and Gonçalves D. 2015. Construction and Building Materials. *Construction and Building Materials* **80**: 155–166.

[9] Yoo, D. Y. and Banthia N. 2019. Impact resistance of fiber-reinforced concrete–A review. *Cement and Concrete Composites* **104**:103389.

[10] Wang S. and Xu L. and Yin C. and Chen Z. and Chi Y. 2021. Experimental investigation on the damage behavior of ultra-high performance concrete subjected to cyclic compression. *Composite Structures* **267**:113855.

[11] Meyer F. 1994. Topographic distance and watershed lines. *Signal processing* **38**:113–125.

[12] Barber C. B. and Dobkin D. P. and Huhdanpaa H. 1996. The quickhull algorithm for convex hulls. *ACM Transactions on Mathematical Software (TOMS)* **22**:469–483.

[13] Geuzaine C. and Remacle J. F. 2009. Gmsh: A 3-D finite element mesh generator with built-in pre-and post-processing facilities. *International Journal for Numerical Methods in Engineering* **79**:1309–1331.

[14] Camacho, G. T. and Ortiz, M. 1996. Computational modelling of impact damage in brittle materials. *International Journal of solids and structures* **33**:2899–2938.

[15] Snozzi, L. and Molinari, J. F. 2013. A cohesive element model for mixed mode loading with frictional contact capability. *International Journal for Numerical Methods in Engineering* **93**:510–526.

[16] Oliver J. and Huespe A. E. and Cante J. C. 2008. An implicit/explicit integration scheme to increase computability of non-linear material and contact/friction problems. *Computer Methods in Applied Mechanics and Engineering* **197**:1865–1889.

[17] Paulino, G. H. and Celes, W. and Espinha, R. and Zhang, Z. 2008. A general topology-based framework for adaptive insertion of cohesive elements in finite element meshes. *Engineering with Computers* **24**:59–78.

[18] Oñate E. 2013. *Structural analysis with the finite element method. Linear statics: volume 2: beams, plates and shells*, Springer Science & Business Media.

[19] Hughes T.J.R. 1987. *The Finite Element Method: Linear Static and Dynamic Finite Element Analysis*, Prentice-Hall, Inc.

[20] Leung C.K.Y. and Chi J. 1995. Crack-bridging force in random ductile fiber brittle matrix composites. *Journal of Engineering Mechanics* **121**:1315–1324.

[21] Van Mier, J. G. M. 2012. *Concrete fracture: a multiscale approach*, CRC press.

[22] Oneschkow N. and Timmermann T. 2022. Influence of the composition of high-strength concrete and mortar on the compressive fatigue behaviour. *Materials and Structures* **55**:83.

[23] Van Mier, J. G. M. 1996. *Fracture processes of concrete*, CRC press.

[24] Simo, J. C. and Hughes T. J. R. 1998 *Computational inelasticity*, Springer Science & Business Media.